ACS OMEGA

http://pubs.acs.org/journal/acsodf

Article

Mesoporous Activated Carbon from Leaf Sheath Date Palm Fibers by Microwave-Assisted Phosphoric Acid Activation for Efficient Dye Adsorption

Hattan A. Alharbi, Bassim H. Hameed, Khaled D. Alotaibi,* Saud S. Aloud, and Abdullah S. Al-Modaihsh

Cite This: *ACS Omega* 2022, 7, 46079−46089

Read Online

ACCESS | Metrics & More | Article Recommendations

ABSTRACT: Remazol Brilliant Blue R (RBBR) is a common dye used in the industry, and its presence in wastewater and discharge into the environment can create a serious concern for the ecosystem and human health. Activated carbon produced from crop residues has emerged as a promising technique for removing contaminants from wastewater. In this study, leaf sheath date palm fiber-based activated carbon (LSDAC) was synthesized via phosphoric acid, H_3PO_4, treatment, followed by a microwave-induced carbonization process. The produced LSDAC was found to have a BET surface area of 604.61 m^2/g, a Langmuir surface area of 922.05 m^2/g, a total pore volume of 0.35 cm^3/g, and an average pore size of 2.75 nm. The highest removal of RBBR was achieved at a solution pH of 3 (92.56 mg/g) and a solution temperature of 50 °C (90.37 mg/g). Adsorption of RBBR onto LSDAC followed the Langmuir isotherm model with a maximum monolayer capacity, Q_m, of 243.43 mg/g, whereas in terms of kinetics, this adsorption system was best described by the pseudo-first-order (PFO) model. The calculated thermodynamic parameters $\Delta H°$, $\Delta S°$, $\Delta G°$, and Arrhenius activation energy, E_a, were 4.71 kJ/mol, 0.10 kJ/mol·K, −26.25 kJ/mol, and 5.88 kJ/mol, respectively, indicating that the adsorption of RBBR onto LSDAC was endothermic in nature, exhibited increased randomness at the solid−liquid interface, and was spontaneous and controlled by physisorption.

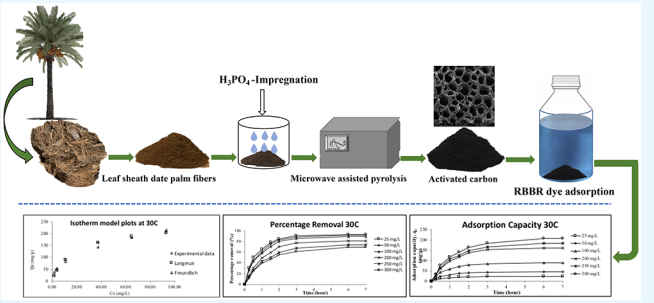

1. INTRODUCTION

Water contamination with textile dyes from industrial effluents has been one of the never-ending global issues. Dyes that bypass the inefficient wastewater treatment in textile industries enter the environment and cause harm to living organisms.[1,2] According to,[3] dyes are extensively utilized in many industrial activities namely paper, magazines, foods, cosmetics, leather, and much more. Therefore, it is not a surprise that the annual generation of dyes contained in wastewater from the textile industry alone has reached 2.15 billion tons.[4,5] Based on the solubility properties, dyes can be grouped into soluble dyes (acidic, basic, reactive, and direct dyes) and insoluble dyes (vat, sulfur, disperse, and pigment dyes).[6,7] According to,[8] soluble dyes are harder to be removed due to their strong affinity toward the polar region of water molecules. Remazol Brilliant Blue R (RBBR) is one of the popular dyes in the textile industry, and it falls in the group of reactive dyes. Reactive dyes dissociate in water to produce negative ions (anionic dyes) and attach to the fiber substrate via covalent bonds. Up to 70% of the reactive dyes share similar characteristics of having at least one azo bridge (−N═N−) on their molecular structure.[9] It is an absolute need for researchers to treat reactive dyes in wastewater since this class of dyes ends up in discharged effluents, most of which are around 10−50%.[10]

Activated carbon (AC) is a versatile and reliable adsorbent for treating a wide range of water-based pollutants such as dyes,[11−14] heavy metals,[15−18] antibiotics,[19,20] pesticides,[21,22] and much more. This outstanding trait of AC is attributed to two main factors: (i) high surface area from a highly porous structure and (ii) the existence of many polar functional groups that enhance the attraction between adsorbate molecules and the AC's surface. However, two decades ago, AC was struggling with the issue of high production costs due to the usage of the nonrenewable precursors coal, lignite, and petroleum coke.[8] Alternatively, researchers have been actively producing AC from agricultural wastes such as *Gelidiella acerosa* seaweed,[11] durian peel,[8] peanut shell,[23] coconut shell,[21] biomass sludge,[24] and *alpinia galanga* stem.[25] Date palm (*Pheonix dactylifera L.*) is a native tree of the Middle East and

Received: June 16, 2022
Accepted: November 22, 2022
Published: December 8, 2022

North African countries, which contribute 88.90% (7,267,316 tons) of the global date fruit production. Other parts of the world such as America and Europe produce 0.58 and 0.18%, respectively.[26] In addition to fruit production, the date palm tree also generates approximately 6 million tons of waste annually.[27] According to,[28] one date palm tree produces about 2−3 kg of dried leaf. Due to the low nitrogen percentage, these wastes are not suitable to be transformed into compost fertilizer, and incinerating them would cause catastrophic air pollution.[29] Therefore, in this study, an attempt was made to transform leaf sheath date palm fibers (LSD) into AC via phosphoric acid chemical treatment, followed by microwave heating. Unlike a conventional furnace that works based on conduction heat transfer, microwave heating is more efficient, as it converts electromagnetic waves into thermal energy in a volumetric state; thus, the heating process can be done way faster.[30]

2. MATERIALS AND METHODS

2.1. Materials. Phosphoric acid (H_3PO_4) was obtained from Sigma-Aldrich, 0.10 M hydrochloric acid (HCl) was obtained from R&M Chemicals, and RBBR dye was purchased from Merck. Nitrogen in the form of N_2 gas with a purity of 99.9% was supplied by MOX Gases Berhad.

2.2. Collection and Preparation of Leaf Sheath Date Palm Fiber-Activated Carbon. Raw leaf sheath date palm fibers (LSD) were collected from a farm near Riyadh city, Saudi Arabia, dried in the open air, chopped into small pieces, and finely ground to pass a 2.0 mm sieve. Then, it was brought to the lab and cleaned properly using tap water and then dried in an oven for 48 h at a temperature of 110 °C. The LSD was impregnated with H_3PO_4 at an impregnation ratio (IR) of 1:3 for 8 h at a temperature of 40 °C. Then, the impregnated LSD was loaded inside a quartz test tube and carbonized using a microwave oven (EMW2001W, Sweden) under the flow of N_2 gas at a radiation power and radiation time of 616 W and 10 min, respectively. The activated LSD was soaked with 0.10 HCl for 30 min, then followed by a washing step until the washing water reached a pH of 6−7. Then, the sample was dried in an oven once again. After that, the dried sample (LSDAC) was stored in an airtight container until used in adsorption studies.

2.3. Characterization Methods. The samples in this study were characterized in terms of surface area (BET and Langmuir) and average pore diameter together with total pore volume utilizing a volumetric adsorption analyzer (Micromeritics ASAP 2020), scanning electron microscopy (SEM) images using a scanning electron microscope (LEO SUPRA 55VP, Germany), elemental analysis using a simultaneous thermal analyzer (Model PerkinElmer STA 6000), proximate analysis using a thermogravimetric analyzer, functional groups through a Fourier transform infrared spectrometer (FTIR) (IR Prestige 21 Shimadzu, Japan) and distribution of ζ-potential via a ζ-potential analyzer (Zetasizer Nano Series DKSH).

2.4. Equilibrium Study. In the equilibrium study, the influence of dissimilar adsorbate initial concentrations, the influence of adsorbate solution temperature, and the influence of adsorbate solution pH were verified. To understand the adsorbent performance under the various initial concentrations of the adsorbate solution, RBBR solution with six different concentrations between 25 and 300 mg/L were made and placed inside conical flasks. These flasks were shaken at 30 rpm in a water bath shaker. A total of 0.2 g of LSDAC was dropped inside each one of these flasks, and other conditions such as solution pH and solution temperature were fixed at the original pH and 30 °C, respectively. The determination of RBBR's concentration was made via UV−vis spectrophotometry (Agilent Cary 60) every 15 min until equilibrium was reached. The wavelength for RBBR was set to 590 nm. To verify the effect of solution temperature, the temperature of the RBBR solution was varied between 30, 40, and 50 °C, while its pH remained unaltered. Meanwhile, the impact of solution pH on the adsorption process was verified by preparing the RBBR solution with six dissimilar pH values, ranging from 3 to 13, by adding NaOH/HCl, while the solution temperature remained unchanged at 30 °C. In these studies, (effect of solution temperature and solution pH), other parameters such as LSDAC weight, the concentration of the solution, the volume of the solution, and shaking speed were fixed at constant values of 0.2 g, 100 mg/L, 200 mL, and 30 rpm, respectively. RBBR uptakes and percentage removal were calculated based on the following equations, respectively

$$q_e = \frac{(C_0 - C_e)V}{M} \tag{1}$$

$$\text{removal}\ (\%) = \frac{(C_0 - C_e)}{C_0} \times 100\% \tag{2}$$

where q_e, C_0, C_e, V, and M are the quantity of RBBR uptakes during the equilibrium state (mg/g), initial concentration of RBBR (mg/L), the concentration of RBBR at the equilibrium state (mg/L), the volume of RBBR solution (mL), and the mass of LSDAC (g), respectively.

2.5. Isotherm Study. Information regarding the adsorbate−adsorbent system can be gathered via the application of isotherm models. Two isotherm models, namely Langmuir and Freundlich, were utilized, and their formulas are presented as follows, respectively[31,32]

$$\text{Langmuir:} q_e = \frac{Q_m K_L C_e}{1 + K_L C_e} \tag{3}$$

$$\text{Freundlich:} q_e = K_F C_e^{1/n_F} \tag{4}$$

where Q_m and K_L are the maximum monolayer adsorption capacity (mg/g) and constant of Langmuir that is related to the energy of adsorption (L/mg), respectively; K_F is the Freundlich adsorption constant $(mg/g)(L/mg)^{1/n}$; n_F is the heterogeneity factor; R is the universal gas constant (8.314 J/mol·K); and T is the temperature (K). These nonlinear models were solved using Microsoft Excel Solver v. 2016. In addition to the correlation coefficient, R^2, root mean squared error (RMSE), was also evaluated to find the best-fitted model. The formula for RMSE is as follows[14]

$$\text{RMSE} = \sqrt{\frac{1}{n-1}\sum_{n=1}^{n}(q_{e,\exp,n} - q_{e,\text{cal},n})^2} \tag{5}$$

2.6. Kinetic Study. In the kinetic study, the same procedures as those in the equilibrium study were conducted with the determination of the RBBR concentration at a predetermined time from t = 0 min until t = 180 min. Two most popular kinetic models, namely pseudo-first order (PFO) and pseudo-second order (PSO), were used in this study. Their equations are given as follows, respectively[33,34]

https://doi.org/10.1021/acsomega.2c03755
ACS Omega 2022, 7, 46079−46089

$$\text{PFO}: q_t = q_e[1 - \exp(-k_1 t)] \quad (6)$$

$$\text{PSO}: q_t = \frac{k_2 q_e^2 t}{1 + k_2 q_e t} \quad (7)$$

where k_1 and k_2 are the PFO rate constant (1/min) and PSO rate constant (g/mg min), respectively. Similar to the isotherm study, the best-fitted kinetic model was chosen based on both R^2 and RSME.

2.7. Mechanism Study. The mechanism study was conducted using two models, namely the intraparticle diffusion model and the Boyd plot model. The equations of these models are given as follows, respectively

$$q_t = K_p t^{1/2} + C \quad (8)$$

$$B_t = -0.4977 - \ln\left(1 - \frac{q_t}{q_e}\right) \quad (9)$$

where K_p is the intraparticle diffusion rate constant (mg/g·$h^{1/2}$), C is the constant related to the boundary layer thickness, and B_t is the mathematical function of q_t/q_e.

2.8. Thermodynamic Study. Under the conditions of different solution temperatures, the adsorption process can be greatly influenced. Therefore, a thermodynamic study has been carried out to disclose important findings such as change of enthalpy, $\Delta H°$, change of entropy, $\Delta S°$, Gibbs free energy, $\Delta G°$, and Arrhenius activation energy, E_a. The parameters $\Delta H°$ (kJ/mol) and $\Delta S°$ (kJ/mol·K) can be computed using Van't Hoff equation as given below

$$\ln K_c = \frac{\Delta S°}{R} - \frac{\Delta H°}{RT} \quad (10)$$

where R is the value of the gas constant (8.314 J/mol·K), T is the solution temperature (K), and K_c is the dimensionless constant of equilibrium, which can be computed using the following equation[35]

$$K_c = \frac{1000(\text{mg/g}) \times K_L \times \text{molecular weight of adsorbate} \times [\text{adsorbate}]°}{\gamma} \quad (11)$$

where [adsorbate]° is the adsorbate's standard concentration and under standard conditions, this parameter becomes 1 mol/L, Υ is the dimensionless coefficient of adsorbate's activity, and K_L denotes the adsorption constant for Langmuir (L/mg). $\Delta G°$ (kJ/mol) and E_a (kJ/mol) can be determined from the following formulas, respectively

$$\Delta G° = H° - TS° \quad (12)$$

$$\ln k_2 = \ln A - \frac{E_a}{RT} \quad (13)$$

where k_2 and A are the rate constant for PSO (g/mg min) and Arrhenius factor, respectively.

3. RESULTS AND DISCUSSION

3.1. Characteristics of the Samples. Figure 1 shows the BET surface plot, while Table 1 shows the surface area and pore characteristics of the samples. Based on Table 1, LSDAC was revealed to exhibit a surface area (BET and Langmuir) of 604.61 and 922.05 m^2/g, respectively. The formation of these surface areas was aided by H_3PO_4 acid. According to,[36] the dielectric properties in H_3PO_4 acid boost the degradation of organic components inside the AC by microwave heating. By comparison, the surface area in LSDAC was low compared to that in the work done by[37] where they managed to produce H_3PO_4 activated date stone-based AC with a higher surface area of 1123 m^2/g due to the usage of a higher radiation power of 850 W. Higher radiation power promotes a higher degree of volatilization process, therefore increasing the surface area of the AC. LSDAC has an average pore diameter of 2.75 nm and thus is present in the region of mesopores. Researchers have reported that H_3PO_4 is one of the best chemical agents to produce AC with the dominant mesoporous type of pores, even at relatively low activation temperatures.[38,39]

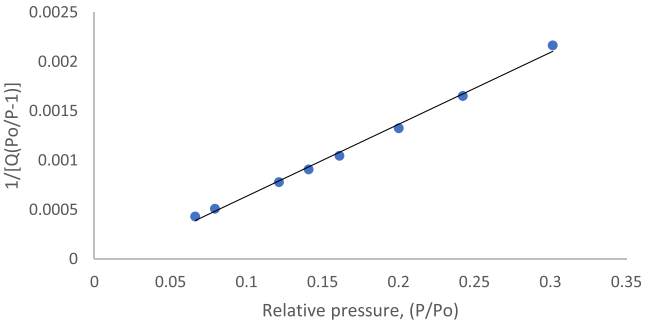

Figure 1. BET surface area plot.

Table 1. BET Surface Area and Pore Characteristics of LSDAC

property	value
BET surface area (m^2/g)	604.61
Langmuir surface area (m^2/g)	922.05
total pore volume (cm^3/g)	0.35
average pore diameter (nm)	2.75

Table 2 lists the elemental and proximate values for LSD and LSDAC. The fixed carbon percentage for LSD was 19.92%, and this percentage was considered to be relatively high and equivalent to that of other biomass reported.[8,13,25] High fixed carbon is a good characteristic of an AC precursor, as the matrices in the AC's structures are made up of fixed carbon. Microwave heating applied in this study succeeded in reducing moisture and volatile matter from 11.92 to 4.26% and from 66.27 to 22.13%, respectively, which subsequently increased fixed carbon tremendously to 69.86%. Effective removal of moisture and volatile matter is crucial to provide spaces for pore network development in LSDAC.

The SEM images for LSD, LSDAC before adsorption of RBBR, and LSDAC after adsorption of RBBR are given in Figure 2a–c, respectively. It can be seen in Figure 2a that the surface of raw LSD was rough and uneven and had an intricate structure. Almost no pores can be detected on its surface. However, after the H_3PO_4 chemical treatment, well-developed pores were formed. Further carbonization using microwave heating induced an enhanced porous structure in LSDAC, as can be seen in Figure 2b. The type of sorption that involves RBBR molecules and the pores on the surface of LSDAC can be verified via isothermal, kinetic, and thermodynamic studies in the following sections.

ζ-potential reflects the net charge of the AC's surface, which directly affects the affinity level of certain adsorbates onto adsorbents.[40] According to,[13] adsorbents with a negative value of ζ-potential provide an enhanced attraction with adsorbates that have a positive net charge and vice versa. Figure 3 presents

https://doi.org/10.1021/acsomega.2c03755
ACS Omega 2022, 7, 46079−46089

Table 2. Elemental and Proximate Analysis of Samples

	elemental analysis					proximate analysis			
samples	C	H	N	S	others	moisture	volatile matter	fixed carbon	ash
leaf sheath fiber (raw)	33.45	3.85	0.97	0.37	61.36	11.92	66.27	19.92	1.90
LSDAC	53.27	3.73	0.88	0.24	41.88	4.26	22.13	69.86	3.75

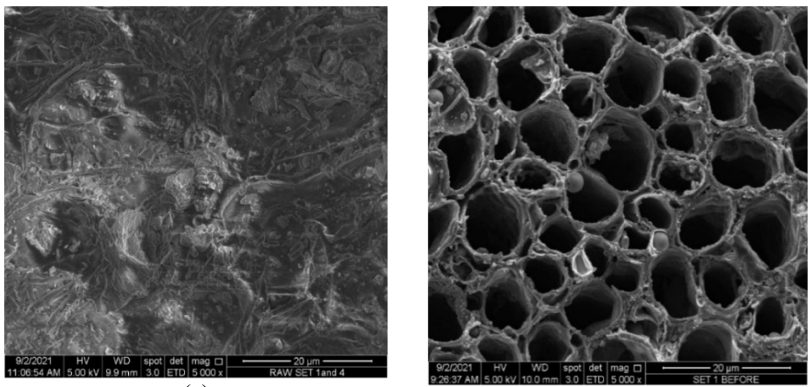

Figure 2. SEM images for (a) raw leaf sheath fibers and (b) LSDAC before adsorption (5000× magnification).

	Mean (mV)	Area (%)	St Dev (mV)
Zeta potential (mV): -0.907	**Peak 1:** -4.06	92.60	6.41
Zeta Deviation (mV): 12.80	**Peak 2:** 38.70	7.40	2.23
Conductivity (mS/cm): 2.33	**Peak 3:** 0.00	0.00	0.00
Result quality: Good			

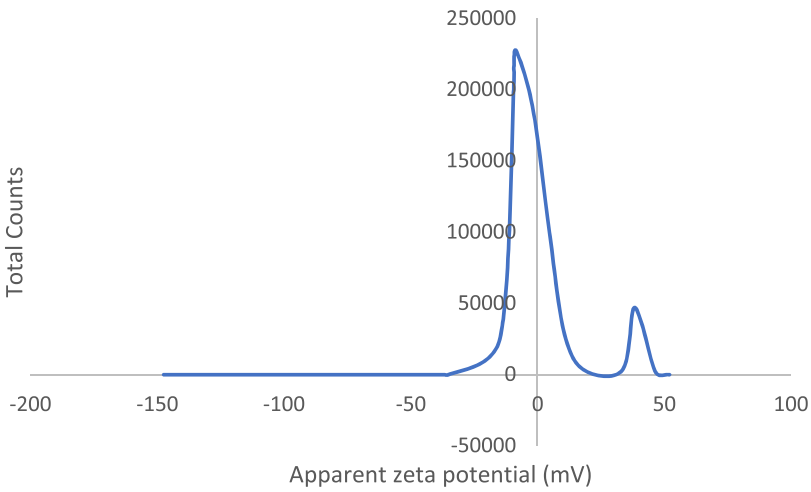

Figure 3. ζ-potential for LSDAC.

the ζ-potential plot for LSDAC, and it was disclosed that the ζ-potential for LSDAC was −0.907 mV. This value indicated that a repulsion force appeared between the negatively charged RBBR ions and LSDAC's surface, therefore signifying that the adsorption of RBBR onto LSDAC was not contributed by electrostatic forces.

Table 3 and Figure 4 show the summary of the FTIR spectrum and plot of the FTIR spectrum, respectively. It was revealed that LSD, LSDAC before adsorption (LSDAC-BA), and LSDAC after adsorption (LSDAC-AA) were found to contain phosphate ions, PO_4^{3-}. The peak for PO_4^{3-} was more intense in LSDAC-BA (1029 cm^{-1}) as compared to that in LSD (1018 cm^{-1}) due to the introduction of H_3PO_4 on the sample during the chemical activation process. However, the intensity of this peak reduced significantly in LSDAC-AA (1072 cm^{-1}) due to the interaction with RBBR molecules. Both LSD and LSDAC-BA were spotted to have aliphatic chloro compounds, C−Cl stretch (771 and 765 cm^{-1}), and aromatic nitro compounds, R-NO (1537 and 1525 cm^{-1}). Several compounds existing in LSD such as tertiary alcohol, O-H bend (1398 cm^{-1}), and alkenyl C═C stretch (1624 cm^{-1}) were noticed to be missing in LSDAC-BA due to their instability toward microwave heating treatment. Owing to the interaction with H_3PO_4 and microwave heating treatments on LSD, few functional groups were developed on LSDAC-BA such as sulfonates (1149 cm^{-1}), aromatic phosphates (1232

https://doi.org/10.1021/acsomega.2c03755
ACS Omega 2022, 7, 46079−46089

Table 3. Summary of FTIR Spectra for Samples

precursor		LSDAC-BA		LSDAC-AA	
wavenumber (cm^{-1})	functional groups	wavenumber (cm^{-1})	functional groups	wavenumber (cm^{-1})	functional groups
771	aliphatic chloro compounds, C-Cl stretch	765	aliphatic chloro compounds, C-Cl stretch	999	aliphatic phosphate, P-O-C stretch
1018	phosphate ions, PO_4^{3-}	1029	phosphate ions, PO_4^{3-}	1072	phosphate ions, PO_4^{3-}
1398	tertiary alcohol, O-H bend	1149	sulfonate	1460	methyl C-H asymmetric stretch
1537	aromatic nitro compound, R-NO	1232	aromatic phosphates, P-O-C	1633	alkenyl C=C stretch
1624	alkenyl C=C stretch	1525	aromatic nitro compound, R-NO	2557	thiols, S-H stretch
		3280	hydroxy group, O-H stretch	3257	hydroxy group, O-H stretch
		3323	imino compounds, =N-H stretch		

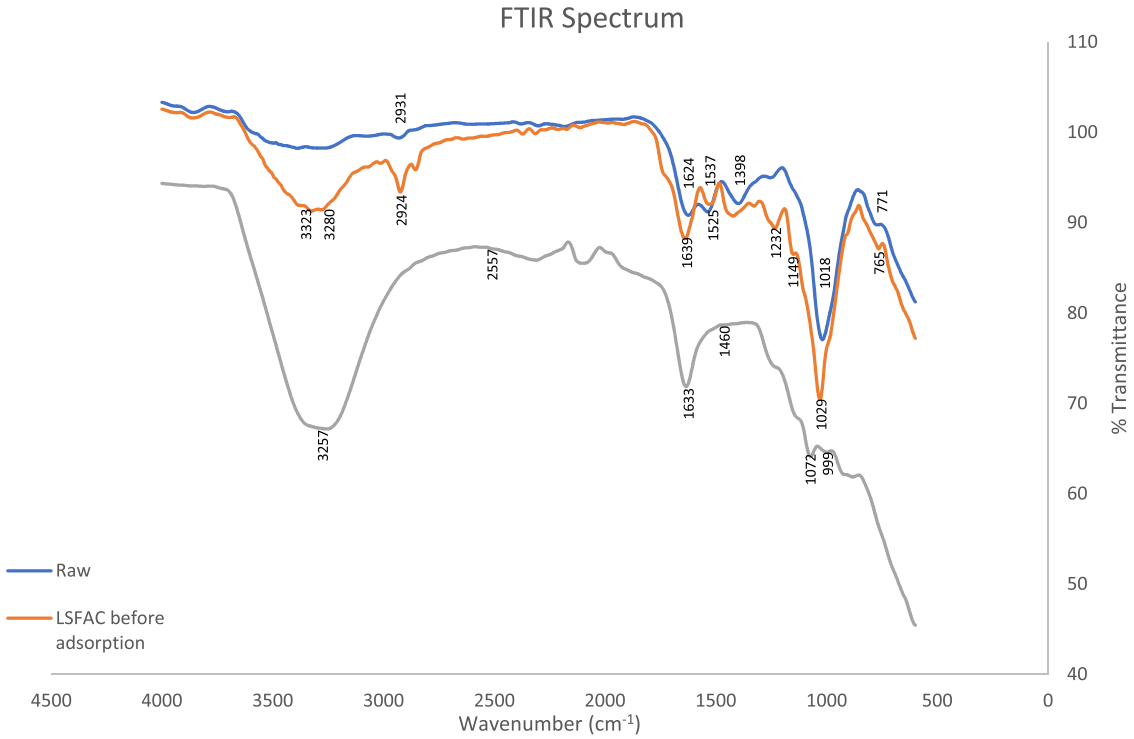

Figure 4. FTIR spectra for raw LSD, LSDAC before adsorption (LSDAC-BA), and LSDAC after adsorption (LSDAC-AA).

cm^{-1}), hydroxy group, OH^- stretch (3280 cm^{-1}), and imino compound, =N−H stretch (3323 cm^{-1}). Among these groups, only the hydroxy group, O−H stretch, survived in LSD-AA (3257 cm^{-1}), whereas other groups were altered into becoming other compounds, due to the interaction with RBBR ions. For instance, sulfonates were transformed into thiols, S−H stretch (2557 cm^{-1}), and aromatic phosphates were reduced to aliphatic phosphates, P−O−C stretch (999 cm^{-1}). The imino compound, =N−H stretch (3323 cm^{-1}), was spotted to form on LSDAC-BA due to the interaction between the N_2 gas introduced during the microwave carbonization process and the LSDAC surface. However, after adsorption, LSDAC-AA lost its imino compound and developed a methyl C−H asymmetric stretch (1460 cm^{-1}) and alkenyl C=C stretch (1633 cm^{-1}).

3.2. Adsorption Equilibrium. The plot of RBBR adsorption capacity versus adsorption time is given in Figure 5a, while the plot of RBBR removal percentage versus adsorption time is provided in Figure 5b. Based on these figures, it can be seen that both the adsorption capacity and percentage removal of RBBR increased with time steadily from 0 to 3 h. At the beginning of the adsorption process, LSDAC was able to provide numerous active sites for the occupation of RBBR molecules. Then, the increase of adsorption capacity and percentage removal of RBBR became slower between 4 and 6 h, which was contributed by the reduced number of available active sites. Furthermore, at this stage, repulsion between RBBR molecules in the bulk phase and solid phase started to occur. From 6 to 7 h, no further increase occurred, thus suggesting that an equilibrium phase was achieved. At this phase, no more RBBR molecules can be adsorbed by LSDAC due to the exhaustion of active sites in LSDAC. As the initial concentration of RBBR increased from 25 to 300 mg/L, the adsorption capacity increased as well from 23.12 to 206.78 mg/g. According to,[41] the more massive driving force of mass transfer is created in the adsorbate solution with thicker concentration, which can triumph mass transfer resistance rather easily, therefore resulting in higher adsorption capacity of the adsorbate. On the contrary, the highest percentage removal of RBBR (92.48%) occurred at the lowest initial concentration of 25 mg/g and vice versa. This phenomenon occurred because at higher initial concentrations, the ratio of

https://doi.org/10.1021/acsomega.2c03755
ACS Omega 2022, 7, 46079−46089

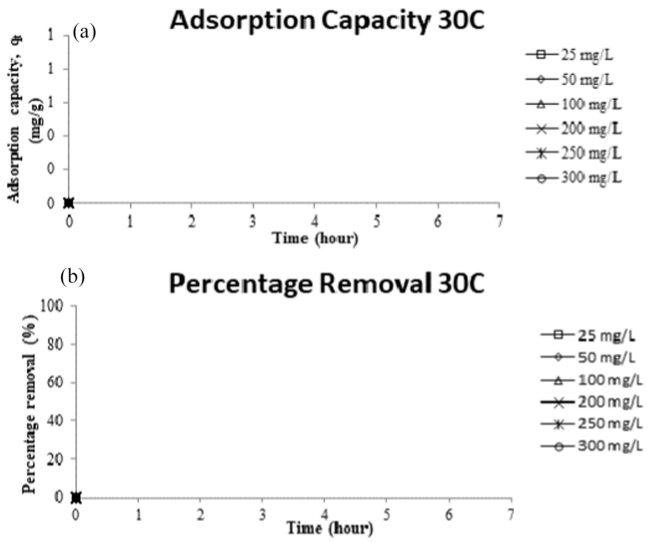

Figure 5. Plots of (a) adsorption capacity and (b) percentage removal of RBBR onto LSDAC versus time at 30 °C for different initial concentrations of RBBR (original pH of RBBR, 0.2 g adsorbent dosage, and 200 mL of solution).

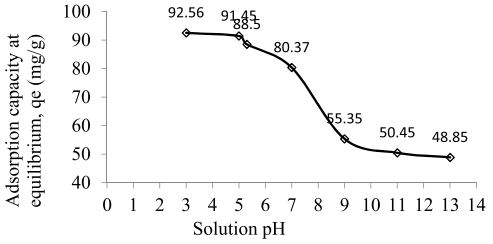

Figure 6. Plots of adsorption capacity of RBBR onto LSDAC versus different solution pH values at 30 °C (100 mg/L initial concentration, 0.2 g adsorbent dosage, and 200 mL of solution).

active sites on LSDAC to RBBR molecules was higher. As the RBBR initial concentration increased, this ratio decreased and caused the percentage removal of RBBR to drop as well.

Figure 6 shows the adsorption uptakes of RBBR by LSDAC under different solution pH values between 3 and 13. The lowest amount of RBBR removed (48.85 mg/g) was acquired at pH 13, signifying that RBBR adsorption onto LSDAC does not favor alkaline conditions. As the solution pH reduced to 11 and 9, the adsorption capacity slightly increased to 50.45 and 55.35 mg/g, respectively. Under these alkaline conditions, RBBR ions had to compete with excess OH^- ions to be adsorbed by the active sites on LSDAC's surface. A significant increase of 80.37 mg/g had occurred at a pH of 7 due to the reduction of OH^- in the RBBR solution, thus reducing the adsorption competition tremendously. At an acidic pH of 5.3 (original pH of the RBBR solution), the existence of H^+ had exerted an inductive effect on the LSDAC's surface to make it positively charged. As the result, RBBR ions' attraction toward LSDAC's surface increased, causing higher adsorption capacity. By increasing the solution pH to 5 and 3, no significant increase can be noticed, as the inductive effect of H^+ ions on LSDAC's surface had reached its maximum potential. At extremely high or extremely low pH values, the solution pH posed a very minimal influence on the adsorption capacity.

3.3. Adsorption Isotherms. Adsorption data were fitted on two isotherm models, namely Langmuir and Freundlich.

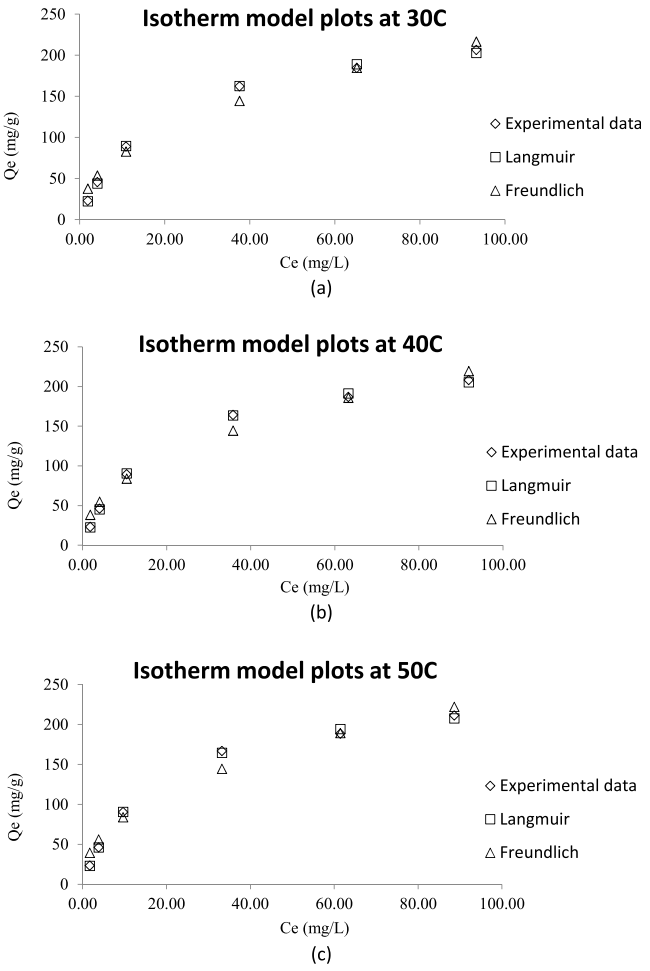

Figure 7. Isotherm plots for the RBBR−LSDAC adsorption system at (a) 30 °C, (b) 40 °C, and (c) 50 °C (original pH of RBBR solution, 0.2 g adsorbent dosage, and 200 mL of solution).

Table 4. Isotherm Parameters for the RBBR−LSDAC Adsorption System

isotherm	parameters	30 °C	40 °C	50 °C
Langmuir	Q_m	243.43	245.31	246.72
	K_L	0.0536	0.0556	0.0600
	R^2	0.9961	0.9960	0.9955
	RSME	2.55	2.23	2.91
Freundlich	K	28.55	29.57	31.19
	n	2.24	2.26	2.28
	R^2	0.9980	0.9979	0.9978
	RSME	11.12	11.98	12.99

Table 5. Comparison of RBBR Adsorption Capacities by Various Biomass-Based AC

precursor	adsorption capacity (mg/g)	references
LSD	246.72	this study
coconut shell	35.09	(Hii, 2021)[43]
coconut shell	8.01	(Lai, 2021)[44]
date pits	105.50	(Thiam et al., 2020)[45]
guava leaf powder	93.12	(Debamita et al., 2020)[46]
orange peel	384.62	(Khasri et al., 2019)[47]

https://doi.org/10.1021/acsomega.2c03755
ACS Omega 2022, 7, 46079−46089

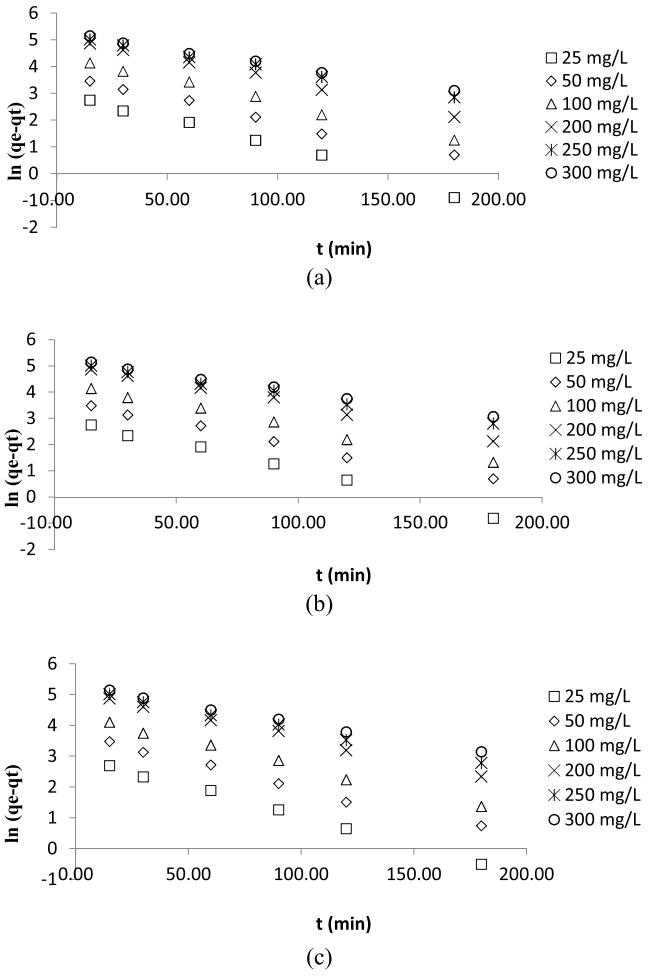

Figure 8. Plots of pseudo-first-order kinetic model for the RBBR–LSDAC adsorption system at solution temperatures of (a) 30 °C, (b) 40 °C, and (c) 50 °C (original pH of RBBR solution, 0.2 g adsorbent dosage, and 200 mL of solution).

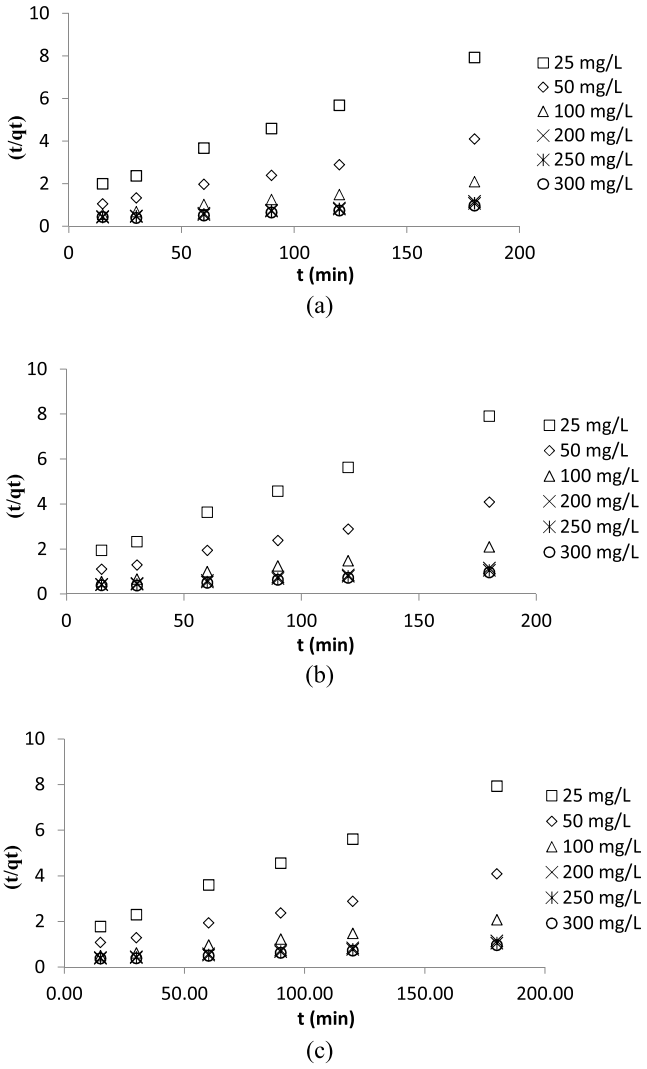

Figure 9. Plots of pseudo-second-order kinetic model for the RBBR–LSDAC adsorption system at solution temperatures of (a) 30 °C, (b) 40 °C, and (c) 50 °C (original pH of RBBR solution, 0.2 g adsorbent dosage, and 200 mL of solution).

The plots of these isotherms together with the values of their parameters are provided in Figure 7 and Table 4, respectively.

It was found that the Langmuir model described the RBBR–LSDAC adsorption system the best due to the high R^2 values (>0.9955) and low RSME values between 2.23 and 2.91, which signified relatively low errors between the predicted and experimental results. Based on the Langmuir model assumptions, adsorption of RBBR onto LSDAC formed a monolayer coverage with a maximum monolayer adsorption capacity, Q_m, of 243.43, 245.31, and 246.72 mg/g at adsorption temperatures of 30, 40, and 50 °C, respectively. At higher adsorption temperatures, the diffusion rate of RBBR molecules into the external boundary layer increased and the intraparticle diffusion of RBBR into the LSDAC's pores got more intense.[42] To further verify the impact of adsorption temperature on the RBBR–LSDAC adsorption performance, a thermodynamic study was conducted, as shown in Section 3.5. The Freundlich heterogeneity factor, n, was found to be between 2.24 and 2.28, and since it was between 1 and 10, it implied a favorable adsorption process. Table 5 shows the comparison of RBBR dye adsorption capacities by biomass-based AC from previous studies. It can be concluded that the performance of LSDAC in adsorbing was competitive as compared to that of other ACs. This may be caused by the high surface area, existence of many functional groups, and mesoporous type of pores in LSDAC.

3.4. Adsorption Kinetics. The kinetic plots of the pseudo-first-order (PFO) model are displayed in Figure 8, while pseudo-second-order (PSO) ones are shown in Figure 9, and the summary of these models' parameters is tabulated in Table 6. On average, both PFO and PSO produced excellent R^2 values of 0.9812 and 0.9931, respectively. However, only PFO produced a relatively low RSME of 7.92 as compared to that of PSO of 51.45, thus signifying that PFO fitted the kinetic data the best and was able to predict actual data with less error. PFO gave an insight that the rate-limiting step involved in the adsorption of RBBR onto LSDAC was contributed by physisorption. A similar case was observed in methyl chloride adsorption by AC.[48] Rate constants from both PFO and PSO were found to decrease from 0.0215 to 0.0122 min^{-1} and from 0.00094 to 0.00004 g mg^{-1} min^{-1}, respectively, as the initial concentration of RBBR increased from 25 to 300 mg/L. At higher concentrations, competition among RBBR molecules for active sites makes the adsorption process slower, thus producing a smaller rate constant.

https://doi.org/10.1021/acsomega.2c03755
ACS Omega 2022, 7, 46079–46089

Table 6. Kinetic Parameters for the RBBR−LSDAC Adsorption System

			pseudo-first order (PFO)					pseudo-second order (PSO)				
	initial RBBR concentration (mg/L)	q_e, exp (mg/g)	q_e, cal (mg/g)	k_1 (min^{-1})	R^2	Δq_t (%)	RSME	q_e, cal (mg/g)	k_2 (g mg^{-1} min^{-1})	R^2	Δq_t (%)	RSME
30 °C	25	23.12	22.53	0.0215	0.9914	2.57		27.70	0.00094	0.9986	19.81	
	50	45.89	39.66	0.0170	0.9932	13.58		55.25	0.00041	0.9973	20.39	
	100	89.15	81.98	0.0176	0.9125	8.04		108.70	0.00020	0.9977	21.92	
	200	162.42	172.12	0.0166	0.9962	5.97		232.56	0.00005	0.9937	43.18	
	250	184.88	178.63	0.0129	0.9975	3.38		250.00	0.00005	0.9941	35.22	
	300	206.78	194.42	0.0122	0.9965	5.98		285.71	0.00004	0.9771	38.17	
	average				**0.9812**	**6.59**	**7.92**			**0.9931**	**29.79**	**51.45**
40 °C	25	23.20	21.89	0.0211	0.9946	5.63		27.62	0.00097	0.9985	19.07	
	50	45.97	39.52	0.0171	0.9932	14.04		55.56	0.00041	0.9973	20.85	
	100	89.53	78.75	0.0172	0.9953	12.04		107.53	0.00021	0.9978	20.10	
	200	164.22	172.53	0.0166	0.9951	5.06		227.27	0.00006	0.9960	38.40	
	250	186.79	177.29	0.0133	0.9958	5.08		250.00	0.00005	0.9917	33.84	
	300	208.15	195.04	0.0124	0.9971	6.30		277.78	0.00004	0.9879	33.45	
	average				**0.9952**	**8.03**	**9.04**			**0.9949**	**27.62**	**47.00**
50 °C	25	23.29	19.63	0.0193	0.9985	15.73		26.95	0.00111	0.9989	15.73	
	50	46.17	39.11	0.0168	0.9923	15.29		55.25	0.00042	0.9976	19.66	
	100	90.37	74.73	0.0166	0.9965	17.31		105.26	0.00025	0.9982	16.48	
	200	166.79	163.47	0.0153	0.9963	1.99		222.22	0.00006	0.9950	33.23	
	250	188.54	177.70	0.0134	0.9971	5.75		250.00	0.00005	0.9956	32.60	
	300	211.36	193.79	0.012	0.9968	8.31		277.78	0.00004	0.9932	31.42	
	average				**0.9963**	**10.73**	**11.14**			**0.9964**	**24.86**	**43.93**

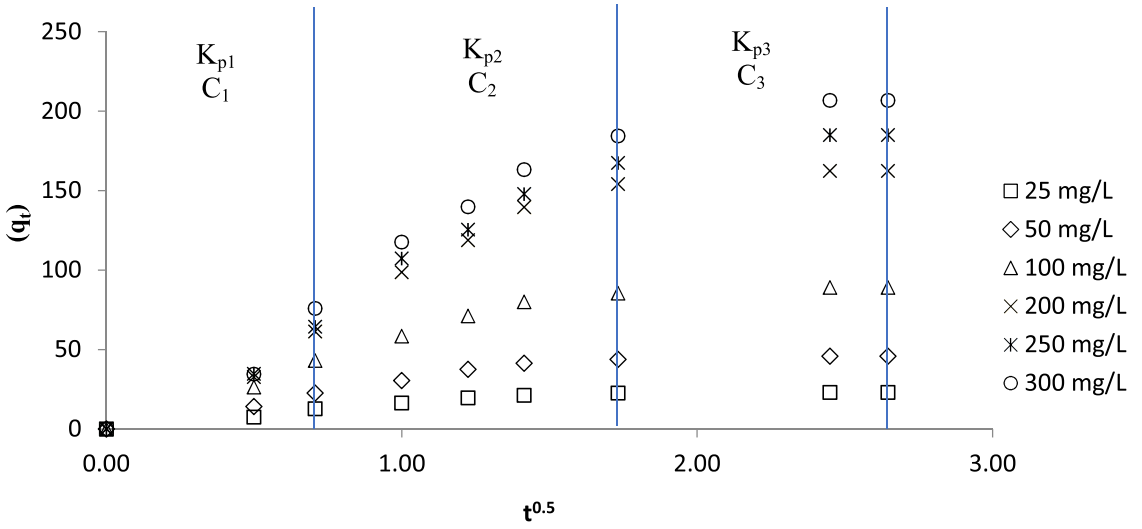

Figure 10. Plots of the intraparticle diffusion model for RBBR adsorption onto LSDAC.

Table 7. Intraparticle Diffusion Parameters

RBBR initial concentration (mg/L)	K_{p1}	K_{p2}	K_{p3}	C_1	C_2	C_3	R_1^2	R_2^2	R_2^3
25	17.38	12.27	0.48	−0.27	4.10	21.89	0.9837	0.9909	0.9584
50	31.24	27.30	2.37	−0.33	3.36	39.82	0.9921	0.9951	0.9584
100	59.60	52.72	4.15	−0.76	5.97	78.53	0.9887	0.9991	0.9584
200	82.73	109.43	9.72	−1.94	−14.30	137.55	0.9629	0.9949	0.9584
250	87.04	115.40	20.49	−2.00	−14.17	132.43	0.9645	0.9868	0.9584
300	100.19	121.85	26.26	−3.51	−8.28	139.56	0.9208	0.9946	0.9584

3.5. Adsorption Mechanisms. The intraparticle diffusion plot is shown in Figure 10, while the respective data are given in Table 7. The plots for all RBBR concentrations studied did not form a straight line and did not pass through the origin. Therefore, the rate-limiting step in the RBBR−LSDAC adsorption system was not caused by intraparticle diffusion. Based on Figure 10, the plot was spotted to be multilinear with three different regions. The first region (t = 0 h until t = 0.5 h) was fast and driven mostly by strong electrostatic attraction.[49] The second region (t = 0.5 h until t = 2 h) was known as the gradual adsorption stage, where the rate-limiting step was mainly contributed by intraparticle diffusion.[50] The last region

https://doi.org/10.1021/acsomega.2c03755
ACS Omega 2022, 7, 46079−46089

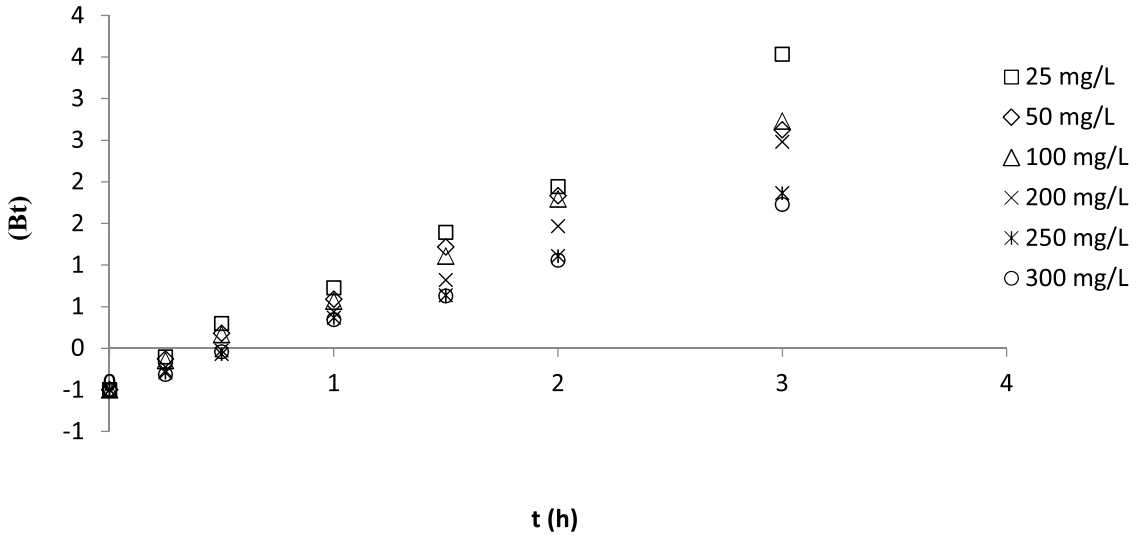

Figure 11. Boyd plot model for RBBR adsorption onto LSDAC.

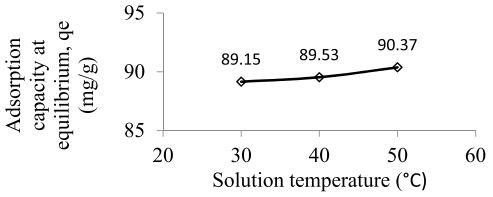

Figure 12. Plots of adsorption capacity of RBBR onto LSDAC versus different solution temperatures (original pH of RBBR solution, 100 mg/L initial concentration, 0.2 g adsorbent dosage, and 200 mL of solution).

Table 8. Thermodynamic Parameters

temperature (K)	ΔH° (kJ/mol)	ΔS° (kJ/mol K)	E_a (kJ/mol)	ΔG° (kJ/mol)
303.15	4.71	0.10	5.88	−26.25
313.15				−27.27
323.15				−28.29

was the final equilibrium phase, where the slowing down of intraparticle diffusion occurred because the number of RBBR molecules available in the solution was significantly low. To further verify the slowest step in the adsorption process, the Boyd plot was produced and is given in Figure 11. It was revealed that all lines did not pass through the origin, which signified that the rate-limiting step for RBBR adsorption onto LSDAC was the film diffusion.[51]

3.6. Adsorption Thermodynamics. The plot of RBBR adsorption capacity under the influence of different solution temperatures is given in Figure 12, and the thermodynamic parameters are presented in Table 8. Based on Figure 12, the adsorption capacity was revealed to increase from 89.15 to 90.37 mg/g when the solution temperature increased from 30 to 50 °C, therefore implying endothermic behavior. This finding was supported by the positive value of ΔH° (4.71 kJ/mol), which confirmed that the adsorption process was indeed endothermic in nature. The ΔG° values at the temperature of 303.15, 313.15, and 323.15 K were disclosed to be −26.25, −27.27, and −28.29 kJ/mol, respectively. The negative sign in this parameter indicates that the adsorption process was spontaneous in nature, and the decrease of this parameter as the temperature increased proved that the adsorption process of RBBR onto LSDAF was favored at a higher temperature. This finding was consistent with Section 3.3, in which at higher temperatures, the Langmuir monolayer adsorption capacity, Q_m, was higher as compared to the low-temperature ones. The ΔS° value was found to be positive, which was 0.10 kJ/mol·K, hence proving the increasing randomness at the solid−liquid interface. Last but not least, the E_a value was revealed to be 5.88 kJ/mol, which signified that the major role of sorption during the rate-limiting step was contributed by physisorption as predicted in Section 3.4.

4. CONCLUSIONS

LSD was successfully converted into LSDAC by employing chemical treatment of H_3PO_4 coupled with microwave heating at 616 W for 10 min. The produced LSDAC was found to be mesoporous with the diameter size of the pores being 2.75 mm and BET surface area being 922.05 m^2/g. By increasing the initial concentration of RBBR, the adsorption capacity of RBBR was found to increase as well, whereas the respective percentage removal was revealed to decrease. Adsorption of RBBR onto LSDAC was found to be optimum at an acidic pH of 3 (92.56 mg/g) and the highest solution temperature studied, 50 °C (90.37 mg/g). Isothermal together with kinetic studies disclosed that the RBBR−LSDAC adsorption system was best described by the Langmuir model and PFO model, respectively, with a maximum monolayer coverage, Q_m, of 243.43 mg/g. A repulsion between the LSDAC's surface and negatively charged RBBR ions occurred due to the negative ζ-potential of −0.906 mV. The surface of LSDAC was filled with various functional groups such as the aliphatic chloro compound, C−Cl stretch, PO_4^{3-} ions, aromatic phosphates, P-O-C, aromatic nitro, R-NO, hydroxy group, O-H stretch, and imino compound, ═N−H stretch. Thermodynamic parameters suggested that the adsorption of RBBR onto LSDAC was endothermic and spontaneous, exhibited increased randomness at the solid−liquid interface, and was governed by physisorption. Overall, LSD served as a good precursor and LSDAC was competent as an adsorbent to remove RBBR from aqueous solution.

https://doi.org/10.1021/acsomega.2c03755
ACS Omega 2022, 7, 46079−46089

AUTHOR INFORMATION

Corresponding Author

Khaled D. Alotaibi − *Department of Soil Science, College of Food and Agriculture Sciences, King Saud University, Riyadh 11451, Saudi Arabia;* orcid.org/0000-0002-2384-1705; Email: khalotaibi@ksu.edu.sa

Authors

Hattan A. Alharbi − *Department of Plant Protection, College of Food and Agriculture Sciences, King Saud University, Riyadh 11451, Saudi Arabia;* orcid.org/0000-0003-3297-729X

Bassim H. Hameed − *Department of Chemical Engineering, College of Engineering, Qatar University, Doha, Qatar*

Saud S. Aloud − *Department of Soil Science, College of Food and Agriculture Sciences, King Saud University, Riyadh 11451, Saudi Arabia*

Abdullah S. Al-Modaihsh − *Department of Soil Science, College of Food and Agriculture Sciences, King Saud University, Riyadh 11451, Saudi Arabia*

Complete contact information is available at: https://pubs.acs.org/10.1021/acsomega.2c03755

Notes

The authors declare no competing financial interest.

ACKNOWLEDGMENTS

This project was funded by the National Plan for Science, Technology and Innovation (MAARIFAH), King Abdulaziz City for Science and Technology, Kingdom of Saudi Arabia, Award Number (13-ENV1102-02).

REFERENCES

(1) Tkaczyk, A.; Mitrowska, K.; Posyniak, A. Synthetic organic dyes as contaminants of the aquatic environment and their implications for ecosystems: A review. *Sci. Total Environ.* **2020**, *717*, No. 137222.

(2) Shen, Z. Coordinated environment and economy in coastal development based on industrial wastewater and SO_2 emissions. *J. Coastal Res.* **2020**, *109*, 13−18.

(3) Mahapatra, U.; Chatterjee, A.; Das, C.; Manna, A. K. Adsorptive removal of hexavalent chromium and methylene blue from simulated solution by activated carbon synthesized from natural rubber industry biosludge. *Environ. Technol. Innovation* **2021**, *22*, No. 101427.

(4) Guo, G.; Tian, F.; Zhang, L.; Ding, K.; Yang, F.; Hu, Z.; Liu, C.; Sun, Y.; Wang, S. Effect of salinity on removal performance in hydrolysis acidification reactors treating textile wastewater. *Bioresour. Technol.* **2020**, *313*, No. 123652.

(5) Varjani, S.; Rakholiya, P.; Ng, H. Y.; You, S.; Teixeira, J. A. Microbial degradation of dyes: An overview. *Bioresour. Technol.* **2020**, *314*, No. 123728.

(6) Berradi, M.; Hsissou, R.; Khudhair, M.; Assouag, M.; Cherkaoui, O.; El Bachiri, A.; El Harfi, A. Textile finishing dyes and their impact on aquatic environs. *Heliyon* **2019**, *5*, e02711.

(7) Rathi, B. S.; Kumar, P. S.; Vo, D. V. N. Critical review on hazardous pollutants in water environment: Occurrence, monitoring, fate, removal technologies and risk assessment. *Sci. Total Environ.* **2021**, *797*, No. 149134.

(8) Yusop, M. F. M.; Ahmad, M. A.; Rosli, N. A.; Gonawan, F. N.; Abdullah, S. J. 2021a. Scavenging malachite green dye from aqueous solution using durian peel based activated carbon. *Mal. J. Fund. Appl. Sci.* **2021**, *17*, 95−103.

(9) Meerbergen, K.; Crauwels, S.; Willems, K. A.; Dewil, R.; Van Impe, J.; Appels, L.; Lievens, B. Decolorization of reactive azo dyes using a sequential chemical and activated sludge treatment. *J. Biosci. Bioeng.* **2017**, *124*, 668−673.

(10) Sharma, J.; Sharma, S.; Soni, V. 2021. Classification and impact of synthetic textile dyes on Aquatic Flora: A review. *Reg. Stud. Mar. Sci.* **2021**, *45*, 101802.

(11) Ahmed, M. J.; Okoye, P. U.; Hummadi, E. H.; Hameed, B. H. High-performance porous biochar from the pyrolysis of natural and renewable seaweed (Gelidiella acerosa) and its application for the adsorption of methylene blue. *Bioresour. Technol.* **2019**, *278*, 159−164.

(12) Streit, A. F.; Côrtes, L. N.; Druzian, S. P.; Godinho, M.; Collazzo, G. C.; Perondi, D.; Dotto, G. L. Development of high-quality activated carbon from biological sludge and its application for dyes removal from aqueous solutions. *Sci. Total Environ.* **2019**, *660*, 277−287.

(13) Yusop, M. F. M.; Ahmad, M. A.; Rosli, N. A.; Manaf, M. E. A. Adsorption of cationic methylene blue dye using microwave-assisted activated carbon derived from acacia wood: Optimization and batch studies. *Arabian J. Chem.* **2021**, *14*, No. 103122.

(14) Marrakchi, F.; Hameed, B. H.; Bouaziz, M. Mesoporous and high-surface-area activated carbon from defatted olive cake by-products of olive mills for the adsorption kinetics and isotherm of methylene blue and acid blue 29. *J. Environ. Chem. Eng.* **2020**, *8*, No. 104199.

(15) Yusop, M. F. M.; Jaya, E. M. J.; Ahmad, M. A. 2022. Single-stage microwave assisted coconut shell based activated carbon for removal of Zn(II) ions from aqueous solution − Optimization and batch studies. *Arabian J. Chem.* **2022**, *15*, 104011.

(16) Khairiah, K.; Frida, E.; Sebayang, K.; Sinuhaji, P.; Humaidi, S. Data on characterization, model, and adsorption rate of banana peel activated carbon (Musa Acuminata) for adsorbents of various heavy metals (Mn, Pb, Zn, Fe). *Data Brief* **2021**, *39*, No. 107611.

(17) Mandal, S.; Calderon, J.; Marpu, S. B.; Omary, M. A.; Shi, S. Q. Mesoporous activated carbon as a green adsorbent for the removal of heavy metals and Congo red: Characterization, adsorption kinetics, and isotherm studies. *J. Contam. Hydrol.* **2021**, *243*, No. 103869.

(18) Yusop, M. F. M.; Jaya, E. M. J.; Din, A. T. M.; Bello, O. S.; Ahmad, M. A. Single-stage optimized microwave-induced activated carbon from coconut shell for cadmium adsorption. *Chem. Eng. Technol.* **2022**, *45*, 1943−1951.

(19) Ahammad, N. A.; Zulkifli, M. A.; Ahmad, M. A.; Hameed, B. H.; Mohd Din, A. T. Desorption of chloramphenicol from ordered mesoporous carbon-alginate beads: Effects of operating parameters, and isotherm, kinetics, and regeneration studies. *J. Environ. Chem. Eng.* **2021**, *9*, No. 105015.

(20) Khanday, W. A.; Ahmed, M. J.; Okoye, P. U.; Hummadi, E. H.; Hameed, B. H. Single-step pyrolysis of phosphoric acid-activated chitin for efficient adsorption of cephalexin antibiotic. *Bioresour. Technol.* **2019**, *280*, 255−259.

(21) Aziz, A.; Nasehir Khan, M. N.; Yusop, M. F. M.; Jaya, E. M. J.; Jaya, M. A. T.; Ahmad, M. A. Single-Stage Microwave-Assisted Coconut-Shell-Based Activated Carbon for Removal of Dichlorodiphenyltrichloroethane (DDT) from Aqueous Solution: Optimization and Batch Studies. *Int. J. Chem. Eng.* **2021**, *2021*, No. 9331386.

(22) Motaghi, H.; Arabkhani, P.; Parvinnia, M.; Asfaram, A. Simultaneous adsorption of cobalt ions, azo dye, and imidacloprid pesticide on the magnetic chitosan/activated carbon@UiO-66 bio-nanocomposite: Optimization, mechanisms, regeneration, and application. *Sep. Purif. Technol.* **2022**, *284*, No. 120258.

(23) Ahmad, M. A.; Yusop, M. F. M.; Zakaria, R.; Karim, J.; Yahaya, N. K. E. M.; Mohamed Yusoff, M. A.; Hashim, N. H. F.; Abdullah, N. S. Adsorption of methylene blue from aqueous solution by peanut shell based activated carbon. *Mater. Today: Proc.* **2020**, *47*, 1246−1251.

(24) Ahmad, M. A.; Yusop, M. F. M.; Awang, S.; Yahaya, N. K. E. M.; Rasyid, M. A.; Hassan, H. Carbonization of sludge biomass of water treatment plant using continuous screw type conveyer pyrolyzer for methylene blue removal. *IOP Conf. Ser.: Earth Environ. Sci.* **2021**, *765*, No. 012112.

(25) Ahammad, N. A.; Yusop, M. F. M.; Mohd Din, A. T.; Ahmad, M. A. Preparation of alpinia galanga stem based activated carbon via

single-step microwave irradiation for cationic dye removal. *Sains Malays.* **2021**, *50*, 2251−2269.
(26) Ortiz-Uribe, N.; Salomón-Torres, R.; Krueger, R. Date Palm Status and Perspective in Mexico. *Agriculture* **2019**, *9*, 15.
(27) Bastidas-Oyanedel, J.-R.; Fang, C.; Almardeai, S.; Javid, U.; Yousuf, A.; Schmidt, J. E. Waste biorefinery in arid/semi-arid regions. *Bioresour. Technol.* **2016**, *215*, 21−28.
(28) Mallaki, M.; Fatehi, R. Design of a biomass power plant for burning date palm waste to cogenerate electricity and distilled water. *Renewable Energy* **2014**, *63*, 286−291.
(29) Bensidhom, G.; Ben Hassen-Trabelsi, A.; Alper, K.; Sghairoun, M.; Zaafouri, K.; Trabelsi, I. Pyrolysis of Date palm waste in a fixed-bed reactor: Characterization of pyrolytic products. *Bioresour. Technol.* **2018**, *247*, 363−369.
(30) Omoriyekomwan, J. E.; Tahmasebi, A.; Dou, J.; Wang, R.; Yu, J. A review on the recent advances in the production of carbon nanotubes and carbon nanofibers via microwave-assisted pyrolysis of biomass. *Fuel Process. Technol.* **2021**, *214*, No. 106686.
(31) Langmuir, I. The adsorption of gases on plane surfaces of glass, mica and platinum. *J. Am. Chem. Soc.* **1918**, *40*, 1361−1403.
(32) Freundlich, H. M. F. Over the adsorption in solution. *J. Phys. Chem. A* **1906**, *57*, 385−471.
(33) Lagergren, S. K. About the Theory of So-called Adsorption of Soluble Substances. *Sven. Vetenskapsakad. Handingarl* **1898**, *24*, 1−39.
(34) Ho, Y. S.; Mckay, G. Sorption of dye from aqueous solution by peat. *Chem. Eng. J.* **1998**, *70*, 115−124.
(35) Lima, E. C.; Hosseini-Bandegharaei, A.; Moreno-Piraján, J. C.; Anastopoulos, I. A critical review of the estimation of the thermodynamic parameters on adsorption equilibria. Wrong use of equilibrium constant in the Van't Hoof equation for calculation of thermodynamic parameters of adsorption. *J. Mol. Liq.* **2019**, *273*, 425−434.
(36) Canales-Flores, R. A.; Prieto-García, F. Taguchi optimization for production of activated carbon from phosphoric acid impregnated agricultural waste by microwave heating for the removal of methylene blue. *Diam. Relat. Mater.* **2020**, *109*, No. 108027.
(37) Hijab, M.; Parthasarathy, P.; Mackey, H. R.; Al-Ansari, T.; Mckay, G. Minimizing adsorbent requirements using multi-stage batch adsorption for malachite green removal using microwave date-stone activated carbons. *Chem. Eng. Process.* **2021**, *167*, No. 108318.
(38) Han, Q.; Wang, J.; Goodman, B. A.; Xie, J.; Liu, Z. High adsorption of methylene blue by activated carbon prepared from phosphoric acid treated eucalyptus residue. *Powder Technol.* **2020**, *366*, 239−248.
(39) Brazil, T. R.; Gonçalves, M.; Junior, M. S. O.; Rezende, M. C. Sustainable process to produce activated carbon from Kraft lignin impregnated with H_3PO_4 using microwave pyrolysis. *Biomass Bioenergy* **2022**, *156*, No. 106333.
(40) Maršálek, R.; Švidrnoch, M. The adsorption of amitriptyline and nortriptyline on activated carbon, diosmectite and titanium dioxide. *Environ. Challenges* **2020**, *1*, No. 100005.
(41) Tharaneedhar, V.; Senthil Kumar, P.; Saravanan, A.; Ravikumar, C.; Jaikumar, V. Prediction and interpretation of adsorption parameters for the sequestration of methylene blue dye from aqueous solution using microwave assisted corncob activated carbon. *Sustainable Mater. Technol.* **2017**, *11*, 1−11.
(42) Saini, J.; Garg, V. K.; Gupta, R. K.; Kataria, N. Removal of Orange G and Rhodamine B dyes from aqueous system using hydrothermally synthesized zinc oxide loaded activated carbon (ZnO-AC). *J. Environ. Chem. Eng.* **2017**, *5*, 884−892.
(43) Hii, H. T. Adsorption Isotherm And Kinetic Models For Removal Of Methyl Orange And Remazol Brilliant Blue R By Coconut Shell Activated Carbon. *Trop. Aqua. Soil Pollut.* **2021**, *1*, 1−10.
(44) Lai, H. J. Adsorption of Remazol Brilliant Violet 5R (RBV-5R) and Remazol Brilliant Blue R (RBBR) from Aqueous Solution by Using Agriculture Waste. *Trop. Aqua. Soil Pollut.* **2021**, *1*, 11−23.
(45) Thiam, A.; Tanji, K.; Assila, O.; Zouheir, M.; Haounati, R.; Arrahli, A.; Abeid, A.; Lairini, S.; Bouslamti, R.; Zerouq, F.; Kherbeche, A. Valorization of Date Pits as an Effective Biosorbent for Remazol Brilliant Blue Adsorption from Aqueous Solution. *J. Chem.* **2020**, *2020*, No. 4173152.
(46) Debamita, C.; Rampal, N.; Gautham, J.; Vairavel, P. Process optimization, isotherm, kinetics, and thermodynamic studies for removal of Remazol Brilliant Blue-R dye from contaminated water using adsorption on guava leaf powder. *Desalin. Water Treat.* **2020**, *185*, 318−343.
(47) Khasri, A.; Jamir, M. R. M.; Ahmad, M. A.*Adsorbent from Orange Peel for Remazol Brilliant Dye Removal: Equilibrium and Kinetic Studies*, AIP Conference Proceedings, 2019; p 020055.
(48) Lad, J. B.; Makkawi, Y. T. Adsorption of Methyl Chloride on Molecular Sieves, Silica Gels, and Activated Carbon. *Chem. Eng. Technol.* **2020**, *43*, 436−446.
(49) Sun, X.; Cheng, P.; Wang, H.; Xu, H.; Dang, L.; Liu, Z.; Lei, Z. Activation of graphene aerogel with phosphoric acid for enhanced electrocapacitive performance. *Carbon* **2015**, *92*, 1−10.
(50) Wang, P.; Ma, Q.; Hu, D.; Wang, L. Removal of reactive blue 21 onto magnetic chitosan microparticles functionalized with polyamidoamine dendrimers. *React. Funct. Polym.* **2015**, *91*−*92*, 43−50.
(51) Yusop, M. F. M.; Aziz, A.; Ahmad, M. A. Conversion of Teak Wood Waste into Microwave-Irradiated Activated Carbon for Cationic Methylene Blue Dye Removal: Optimization and Batch Studies. *Arabian J. Chem.* **2022**, *15*, 104081.

https://doi.org/10.1021/acsomega.2c03755
ACS Omega 2022, 7, 46079−46089